

High-Performance Photodetector and Angular-Dependent Random Lasing from Long-Chain Organic Diammonium Sandwiched 2D Hybrid Perovskite Non-Linear Optical Single Crystal

Rajesh Kumar Ulaganathan, Pradip Kumar Roy, Swapnil Milind Mhatre, Raghavan Chinnambedu Murugesan, Wei-Liang Chen, Man-Hong Lai, Ambika Subramanian, Chang-Yu Lin, Yu-Ming Chang, Stela Canulescu, Alex Rozhin, Chi-Te Liang,* and Raman Sankar*

3D organic-inorganic metal halide perovskites are excellent materials for optoelectronic applications due to their exceptional properties, solution processability, and cost-effectiveness. However, the lack of environmental stability highly restricts them from practical applications. Herein, a stable centimeter-long 2D hybrid perovskite (N-MPDA)[PbBr₄] single crystal using divalent N1-methylpropane-1,3-diammonium (N-MPDA) cation as an organic spacer, is reported. The as-grown single crystal exhibits stable optoelectronic performance, low threshold random lasing, and multi-photon luminescence/multi-harmonic generation. A photoconductive device fabricated using (N-MPDA)[PbBr₄] single crystal exhibits an excellent photoresponsivity ($\approx 124 \text{ AW}^{-1}$ at 405 nm) that is ≈ 4 orders of magnitudes higher than that of monovalent organic spacer-assisted 2D perovskites, such as (BA)₂PbBr₄ and (PEA)₂PbBr₄, and large specific detectivity ($\approx 10^{12}$ Jones). As an optical gain media, the (N-MPDA)[PbBr₄] single crystal exhibits a low threshold random lasing ($\approx 6.5 \mu\text{J cm}^{-2}$) with angular dependent narrow linewidth ($\approx 0.1 \text{ nm}$) and high-quality factor ($Q \approx 2673$). Based on these results, the outstanding optoelectronic merits of (N-MPDA)[PbBr₄] single crystal will offer a high-performance device and act as a dynamic material to construct stable future electronics and optoelectronic-based applications.

1. Introduction

3D halide perovskites have shown exceptional optoelectronic properties, including solid light harvesting,^[1] high absorption coefficient ($\approx 10^5 \text{ cm}^{-1}$),^[2] photoluminescence quantum yield (PLQY) above 90%,^[3] narrow-band emissions,^[4] and low exciton binding energies.^[5] Hybrid halide perovskite materials exhibited good photodetector performance with high photosensitivity and the photodetectivity in the order of $\approx 10^{15}$ Jones.^[6,7] As an optical gain media, hybrid perovskites showed strong lasing features at ultralow-threshold (220 nJ cm^{-2}) with a high-quality factor ($Q \approx 3600$).^[8] However, the instability of 3D perovskites to moisture, light, and heat remains a challenge, which has hampered the long-lasting performance of 3D perovskite materials in solar cells, photodetectors, lasers, and other optoelectronic applications.^[9–15] In recent years, several approaches have been established

R. K. Ulaganathan, R. Sankar
Institute of Physics
Academia Sinica
Taipei 11529, Taiwan
E-mail: sankarraman@gate.sinica.edu.tw

R. K. Ulaganathan, S. Canulescu
Department of Electrical and Photonics Engineering
Technical University of Denmark
2800 Lyngby, Denmark


P. K. Roy, C.-T. Liang
Department of Physics
National Taiwan University
Taipei 10617, Taiwan
E-mail: ctiliang@phys.ntu.edu.tw

S. M. Mhatre, C.-T. Liang
Graduate Institute of Applied Physics
National Taiwan University
Taipei 10617, Taiwan

R. C. Murugesan, A. Rozhin
Aston Institute of Photonic Technologies
Aston University
Birmingham B4 7ET, UK

W.-L. Chen, M.-H. Lai, Y.-M. Chang
Center for Condensed Matter Sciences
National Taiwan University
Taipei 10617, Taiwan

A. Subramanian, C.-Y. Lin
Department of Mechanical Engineering
Chung Yuan Christian University
Taoyuan 32023, Taiwan

 The ORCID identification number(s) for the author(s) of this article can be found under <https://doi.org/10.1002/adfm.202214078>.

DOI: 10.1002/adfm.202214078

to improve the stability of 3D perovskites. This includes encapsulation, stabilizing perovskite structure through chemical engineering, interfacial alteration, doping, and lowering dimensions.^[16–20] Among these approaches, the formation of 2D perovskite materials has been proven to be a potential route to enhance stability. Moreover, the multi-quantum-well (MQW) structure of the 2D hybrid perovskites leads to unique photo-physical properties, such as longer carrier diffusion, enhanced charge transport, and high exciton binding energy. Ruddeldsen-Popper (RP)-phase 2D perovskites are the most frequently used MQW system, formed by the alternative monovalent organic ammonium spacer (quantum wall) and inorganic layers (quantum well).^[21,22] The general formula for the RP-phase 2D perovskite is $A_2A''_{n-1}B_nX_{3n+1}$, where A is the monovalent organic cation (e.g., $C_8H_9NH_3^+$), A'' is the smaller organic cation (e.g., $CH_3NH_3^+$), B is the metal cation (e.g., Pb^{2+}), X is the halide ions, and n is the numbers of perovskite layers. The “n” regulates the width of the quantum well arrangement, thus leading to a strong exciton creation with high binding energies.^[23]

In 2D hybrid perovskites, the replacement of monovalent organic spacer into divalent organic diammonium cation typically leads to the formation of Dion-Jacobson (DJ)-phase 2D perovskites with a general formula, $A'A_{n-1}B_nX_{3n+1}$ (A' = 3-(aminomethyl)piperidinium (3 AMP) or 4-(aminomethyl)piperidinium (4 AMP), etc.). In contrast to 2D RP perovskites, the van der Waals gap between the adjacent inorganic layers of DJ perovskites is eliminated by the organic diammonium cation, which in turn makes this class of materials more stable for photovoltaics and optoelectronic applications compared to RP phase counterparts.^[24] Using 2D DJ hybrid perovskites, a stable broadband white light emission, solar cells, LEDs, and self-powered ferroelectric photodetectors were reported.^[25–27]

Dohner et al. reported a stable broad white light emission and blue band emission from 2D (N-MEDA)[PbBr₄] and (N-MPDA)[PbBr₄] hybrid perovskite microcrystalline powders, and that was primarily focused on the white light emissive N-MEDA broad band perovskite.^[28] The strong blue band emission and outstanding stability due to the organic long chain diammonium spacer of 2D (N-MPDA)[PbBr₄] hybrid perovskite make it attractive for optoelectronics. In this study, stable photo-detector and random lasing performances are demonstrated from the blue band emissive self-assembled 2D (N-MPDA)[PbBr₄] hybrid perovskite large-size single crystal. Hybrid perovskites in a single crystal form are beneficial because they offer lesser grain boundaries, fewer defects, and longer carrier diffusion.^[29] The centimeter-long single crystal was grown using slow evaporation at constant temperature (SECT), a solution growth method.^[30] The as-grown (N-MPDA)[PbBr₄] single crystal exhibits good stability under an atmospheric

environment and laser illumination; also, it reveals an excellent photoresponsivity of $\approx 124 \text{ A W}^{-1}$ and a high specific detectivity of $\approx 10^{12}$ Jones under blue laser illumination (405 nm). Intriguingly, the as-grown (N-MPDA)[PbBr₄] single crystal also performs as an optical gain resonator for random lasing at a low threshold of $6.5 \mu\text{J cm}^{-2}$. The lasing mode was further evaluated with different angles, which confirms the solid lasing action in different directions. Moreover, the multi-photon luminescence and nonlinear optical second harmonic generation (SHG) were distinguishably recorded from the as-grown single crystal. These figures of merit demonstrate that (N-MPDA)[PbBr₄] single crystal will potentially play an essential role in the next generation of stable and efficient optoelectronic applications.

2. Results and Discussion

Figure 1a demonstrates the growth steps for synthesizing a large-sized single perovskite crystal (N-MPDA)[PbBr₄]. At first, the long-chain organic spacer N-MPDA and lead oxide chemicals were dissolved in a hydrobromic acid solution and heated up to 130 °C with constant magnetic stirring. The above solution was continuously stirred until a clear homogeneous yellow solution was formed. This supersaturated homogeneous solution allows slow evaporation at a constant temperature for the next step. During slow evaporation, the nucleation allows the excess solute in the supersaturated solution to deposit as tiny flakes. In the final step, the obtained small flake was used as a seed crystal in the same solution to grow a large centimeter size single crystal. During this step, the solution was kept at room temperature, which allowed for slow evaporation over a week to obtain high-quality single crystals in micrometer to centimeter sizes (Figure S1, Supporting Information).^[30] The picture of the harvested (N-MPDA)[PbBr₄] single crystal of size (1 cm length \times 1 cm width \times 0.4 cm height) is shown in Figure 1b. Figure 1c shows the 3D crystal structure of the (N-MPDA)[PbBr₄] single crystal. The single crystallinity and phase purity of the as-grown (N-MPDA)[PbBr₄] perovskite was confirmed by the X-ray diffraction (XRD) study, as shown in Figure 1d. The XRD pattern confirms the formation of repeated solid diffraction peaks corresponding to (00l) lattice planes, which indicates the growth orientation along the c-axis. The crystal structure and space group were identified as Monoclinic and $P2_1/c$, with lattice values of $a = 8.27 \text{ \AA}$, $b = 8.28 \text{ \AA}$, and $c = 20.06 \text{ \AA}$, respectively. Based on the crystallographic study, the long-chain N-MPDA spacer can adequately separate the adjacent inorganic layers along the (001) plane (Figure 1c). Moreover, the N-MPDA would not allow hydrogen bonding between the ammonium group and the adjacent perovskites in the (110) structure, avoiding close contact between the adjacent inorganic layers. The crystal structure of the as-grown (N-MPDA)[PbBr₄] single crystal is consistent with the reported literature.^[28,31] Further selected area electron diffraction (SAED) was examined under transmission electron microscopy (TEM) to evaluate the single crystallinity nature of as-grown (N-MPDA)[PbBr₄] crystal. Figure 1e shows the TEM image of (N-MPDA)[PbBr₄], and the corresponding SAED pattern is displayed in the inset of Figure 1e. The linearly ordered strong diffraction spots further confirm the high single-crystallinity of our perovskites.

C.-Y. Lin
Research Center for Semiconductor Materials and Advanced Optics
Chung Yuan Christian University
Taoyuan 32023, Taiwan

P. K. Roy
University of Chemistry and Technology Prague
Department of Inorganic Chemistry
Technická 5, Prague 6 16628, Czech Republic

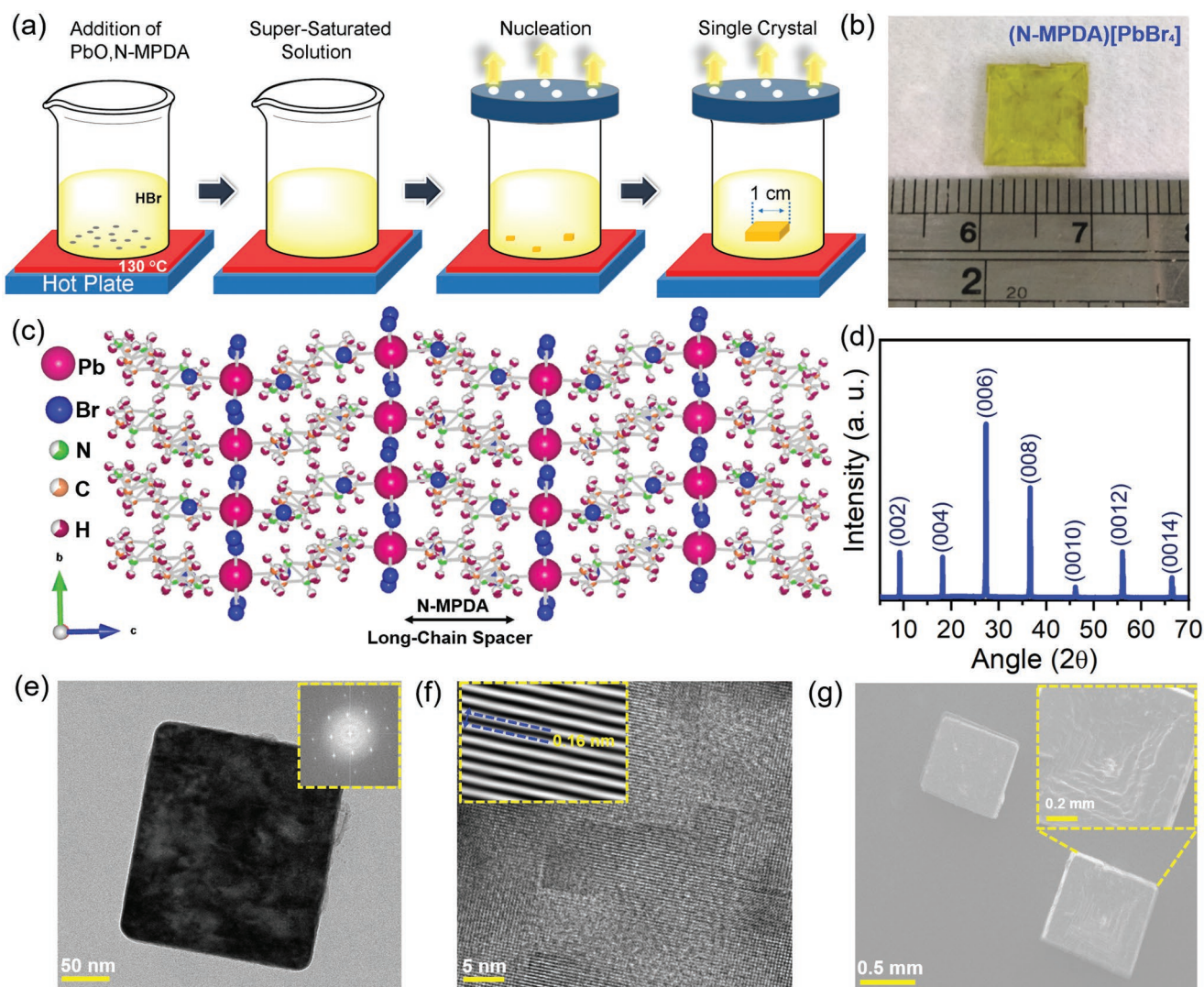


Figure 1. a) Graphical illustration of the slow evaporation at constant temperature (SECT) growth method for the growth of 2D (N-MPDA)[PbBr₄] single crystal. b) Photo image of as-grown centimeter-long single crystal. c) Crystal structure of 2D (N-MPDA)[PbBr₄] hybrid perovskite. d) XRD pattern with indexed miller planes. e) The TEM image and the corresponding SAED pattern are in the inset. f) HR-TEM image with clear lattice fringes and the FFT image of the inset shows a lattice distance of 0.16 nm. g) The surface morphology of the SEM images reveals a pyramid-like surface.

Moreover, from a high-resolution TEM image (Figure 1f), the lattice fringes were clearly identified, and the spacing between the lattice fringes was estimated to be ≈ 0.16 nm. In addition, the crystal morphology and elemental compositions of the (N-MPDA)[PbBr₄] crystal were analyzed by scanning electron microscopy (SEM) and energy-dispersive X-ray spectroscopy (EDX). Figure 1g shows the SEM image of an as-grown (N-MPDA)[PbBr₄] crystal with a size of ≈ 1 mm. The inset in Figure 1g shows the pyramid-like growth patterns during the nucleation, and Figure S2 (Supporting Information) confirms the C, N, Pb, and Br elemental presence.

Figure 2 describes the optical properties of the as-grown (N-MPDA)[PbBr₄] perovskite single crystal. Figure 2a shows the photoluminescence (PL) emission spectra, measured at the excitation wavelength of 405 nm. From Figure 2a, a broad PL emission with the emission maxima centered at the wavelength of 427 nm (corresponding to band gap energy 2.9 eV)

was obtained. No additional PL signals are associated with the quasi-phase impurities, revealing the phase purity of the (N-MPDA)[PbBr₄] single crystal. The optical microscopic image of the top surface of the crystal is shown in Figure S3 (Supporting Information), in which the surface morphology shows the pyramid-like growth pattern as perceived in RP phase-based 2D-MHPs. The corresponding PL image of the crystal displayed in Figure 2b proves uniform strong PL emission over the entire crystal surface. The optical homogeneity of the (N-MPDA)[PbBr₄] single crystal was examined by spatially correlated photoluminescence mapping to assess the optical quality further. The spectral mapping obtained over 64×64 pixels is shown in Figure 2c, and the histogram extracted to reveal the distribution of PL maxima is shown in Figure 2d. The PL emission spectra are distributed between 420 and 440 nm all over the regions (Figure 2d). The measured PL spectra with mild inhomogeneous tail (inset of Figure 2d) for the 2D (N-MPDA)[PbBr₄]

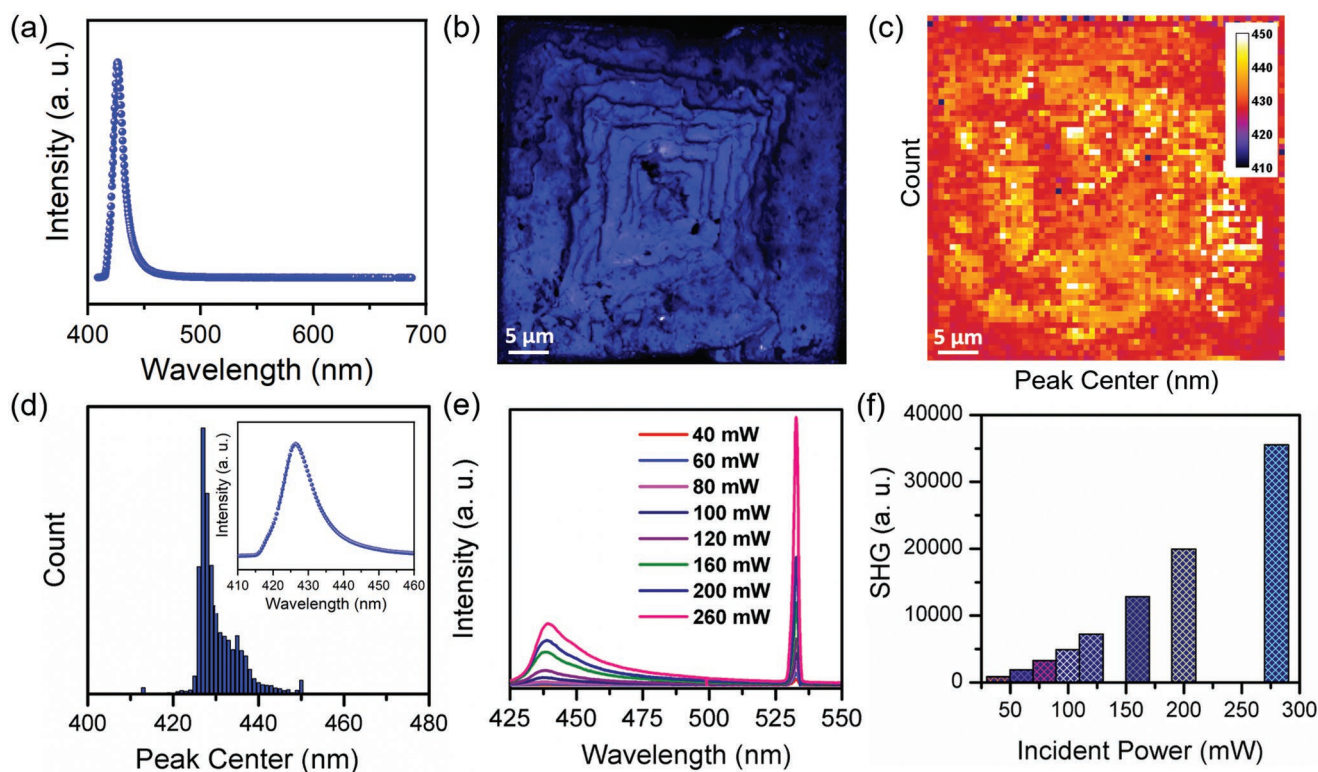


Figure 2. Optical properties of (N-MPDA)[PbBr₄] single crystal: a) The PL spectrum showing emission maxima at 427 nm. b) PL image of the single-crystal perovskite. c) Spatially correlated PL spectral mapping of the (N-MPDA)[PbBr₄] single crystal confirms the spectral uniformity. d) Histogram distribution of emission wavelength maxima of the (N-MPDA)[PbBr₄] single crystal. The inset shows the PL spectrum in the wavelength region shrunk at 410–460 nm. e) The multi-photon PL and SHG were measured at different laser excitation power of the (N-MPDA)[PbBr₄] single crystal. f) The extracted histogram of SHG intensity versus incident power.

hybrid perovskite single crystal are well consistent with the reported literature.^[28] The superposition of band-edge emission along with the sidebands might be attributed to the broad tails in the PL spectra of (N-MPDA)[PbBr₄] single crystal.^[32] The phonon generation or annihilation due to the existence of defects and traps in the large-size single crystal is attributed to the formation of PL sidebands (Figure 2d), which can be observed in a wide variety of perovskite materials.^[33–36]

Nonlinear optical property, especially SHG, is inevitable for the rapid probing of non-centrosymmetric (lacking inversion symmetry) crystalline materials, which typically helps with a preliminary assessment of crystalline material for polar phases, piezoelectric, and ferroelectric applications.^[37,38] The SHG spectroscopic analysis was performed using a 1064 nm femtosecond laser with in-house laser scanning confocal microscopy. The SHG and multi-photon excited PL spectra of the (N-MPDA)[PbBr₄] single crystal under various laser power were acquired and shown in Figure 2e. A double frequency peak at 532 nm and a multi-photon excited PL emission spectrum centered at 437 nm were observed (Figure 2e). The SHG and multi-photon excited PL intensities increase with increasing power and gradually reach the maximum at 280 mW (Figure 2e,f). Based on the crystallographic study, the 2D (N-MPDA)[PbBr₄] perovskite single crystal belongs to the centrosymmetric P21/c space group that typically vanishes second-order nonlinear susceptibility ($\chi^{(2)} = 0$). In contrast, the observed sharp SHG signal at

a high laser power excitation reveals the breaking of inversion symmetry and induced polarizability at the microscopic level. The above result is consistent with the other centrosymmetric 2D hybrid halide perovskite crystal, such as (BA)₂PbI₄ (*Pbca*) and (PEA)₂MAPb₂I₇ (*Pi*) crystals.^[37,38] The photon energy at 1064 and 532 nm is insufficient to complete the bandgap transition of the sample. Therefore, the acquired PL spectra might be attributed to a three-photon excited bandgap transition.

Due to promising optical properties and exceptional stability, we have been motivated to explore (N-MPDA)[PbBr₄] single-crystal for optoelectronic applications, such as a photodetector, and as an optical gain media for laser generation. To fabricate a photoconductive device, a tiny high-quality (N-MPDA)[PbBr₄] crystal was transferred onto a silicon substrate with a 300-nm-thick SiO₂ dielectric layer. Both ends of the crystal were deposited with a gold (Au) electrode of a thickness of ≈ 300 nm with a ≈ 10 -nm-thick chromium (Cr) layer for adhesion using the standard shadow mask technique. **Figure 3a** is the diagrammatic view of a 2D (N-MPDA)[PbBr₄] photodetector under 405 nm laser irradiation. **Figure 3b** shows the source-drain current versus source-drain voltage (I_{ds} - V_{ds}) curve of the (N-MPDA)[PbBr₄] device under the illumination of 405 nm laser with various power densities from 0.15 to 26 mW cm⁻² at $V_{ds} = 0$ to 10 V and $V_g = 0$ V. I_{ds} increase with laser power, showing that more charge carriers are generated at high powers in the channel. The photocurrent ($I_{ph} = I_{light} - I_{dark}$) is calcu-

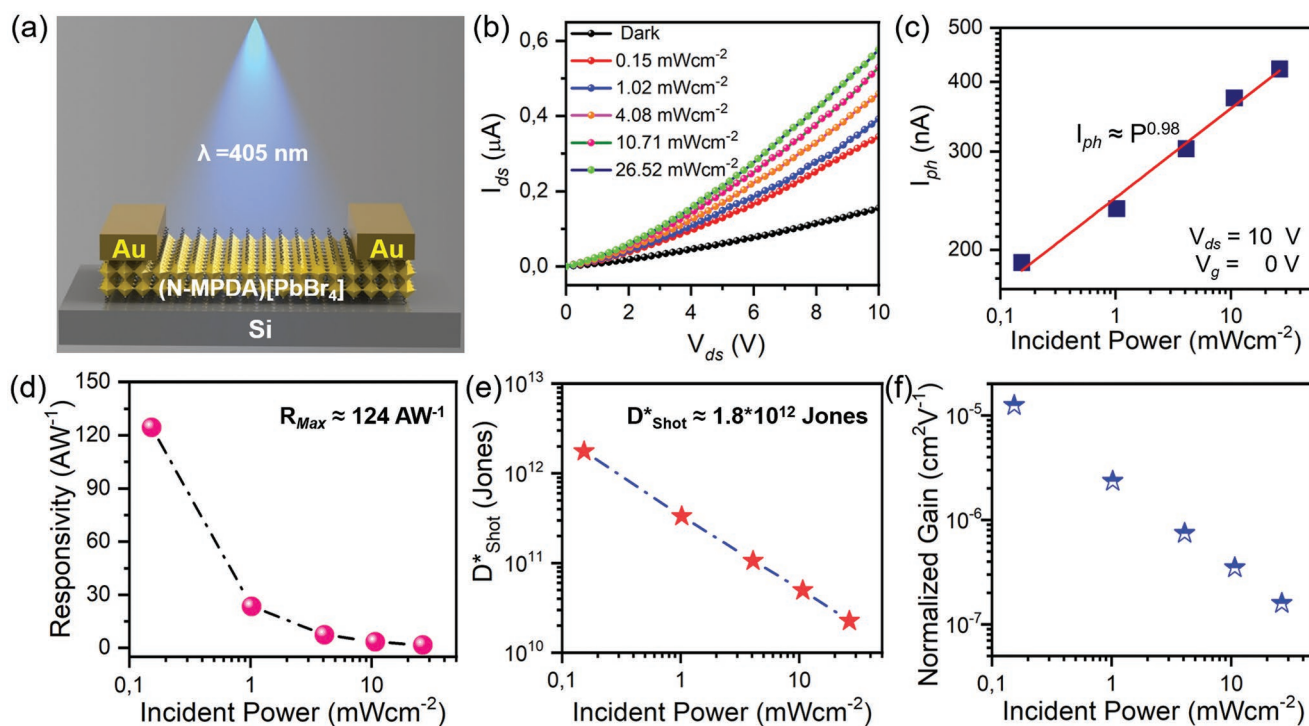


Figure 3. a) The schematic illustration of (N-MPDA)[PbBr₄] single crystal photodetector. b) Output characteristic curves of the photodetector under dark and 405 nm light illumination at $V_g = 0$ V. c) I_{ph} plot is shown with respect to incident laser power at $V_{ds} = 10$ V and $V_g = 0$ V; the data points were fitted and revealed $I_{ph} \approx P^{0.98}$. d) The photoresponsivity of the single crystal under different laser intensities of 405 nm. The (N-MPDA)[PbBr₄] shows a maximum R_λ of 124 A W⁻¹ at 0.15 mW cm⁻², $V_g = 0$ V, and $V_{ds} = 10$ V. e, f) The calculated specific detectivity and normalized gain value for (N-MPDA)[PbBr₄] single crystal at $V_g = 0$ V and $V_{ds} = 10$ V is 1.8×10^{12} Jones and 1.24×10^{-5} V⁻¹ cm².

lated by deducting the light current (I_{light}) from the dark current (I_{dark}) in Figure S4 (Supporting Information). From Figure S4 (Supporting Information), we extracted the I_{ph} at V_{ds} of 10 V and plotted it concerning incident power, which is increasing sub-linearly following the power law of $I_{ph} \approx P^{0.98}$ with the incident powers (Figure 3c). The predominant photosensitivity of an (N-MPDA)[PbBr₄] device is calculated and shown in Figure S5 (Supporting Information) as a ratio of the photocurrent to the dark current. The photocurrent is clearly separated from the dark current, confirming the sensitivity and good noise rejection ability of the (N-MPDA)[PbBr₄] device.

Photoresponsivity (R_λ) is an essential parameter in the photodetector device that shows the sensitivity of a photodetector under the light. R_λ is defined as the number of photocurrents generated per incident photon and expressed by $R_\lambda = I_{ph}/P_\lambda S$, where I_{ph} is the generated photocurrent, P_λ is the incident photon density, and S is the illuminated area of the device.^[39,40] Figure 3d displays the calculated photoresponsivity, which is sublinear with reference to the incident light. Extraordinarily, we have achieved a high photoresponsivity of ≈ 124 A W⁻¹ at 0.15 mW cm⁻² of 405 nm ($V_g = 0$ V and $V_{ds} = 10$ V), and the R_λ increases by raising the V_{ds} from 0 to 10 V (Figure S6, Supporting Information). The routes for the photon-to-electron conversion start from the creation of free electron-hole pairs upon light absorption that efficiently transits between the electrodes, consequently enhancing the photoconductive gain. The responsivity (R_λ) value of the (N-MPDA)[PbBr₄] single crystal is ≈ 4 orders of magnitude higher than that of the recently

reported 2D RP-phase (BA)₂PbBr₄ and (PEA)₂PbBr₄ perovskite single crystals.^[41,42] The comparisons of various materials and current results are summarized in Table S1 (Supporting Information).^[41–47] The structure-property relations of the (N-MPDA)[PbBr₄] single crystal can be correlated to the superior carrier transport properties compared to the (BA)₂PbBr₄ and (PEA)₂PbBr₄ crystals, which in turn helps to improve the photoresponsivity.^[48] According to the DFT study, the degree of asymmetry of the organic spacer has a strong influence on the electronic and optoelectronic properties.^[49] The asymmetric diammonium dication of the N-MPDA spacer makes strong bonding between a spacer and the adjacent inorganic layers in the self-assembled 2D perovskite architecture compared to the 2D RP phase perovskites. This results in increased stability as well as improved charge carrier transport in the (N-MPDA)[PbBr₄] single crystal.^[48,49] Besides, the optical properties are determined by the (MX₆)⁴⁻ an octahedral arrangement in the inorganic layers. The single spacer dication ⁺H₃N-R-NH₃⁺ layer allows stiffer interlayer packing, which allows for less distortion, better alignment, and less displacement of the octahedral [MX₆]⁴⁻ inorganic framework compare with RP-phase perovskite with dual spacer layers.^[50–52]

Next, specific detectivity is calculated with shot noise from the dark current as the dominant contribution. Typically, at the non-zero bias of 10 V, the shot noise plays a major contribution than the Johnson and flicker noises.^[53] Therefore, in this study, we used the shot noise contribution in the dark current for the specific detectivity calculation using $(D^*_{shot}) = R_\lambda \sqrt{A/2qI_{dark}}$,

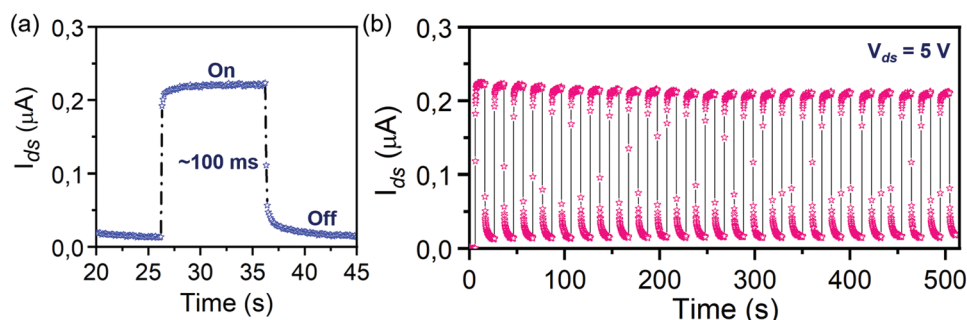


Figure 4. a) Real-time photoresponse curve of the (N-MPDA)[PbBr₄] single crystal under ON/OFF light illumination; the response speed is estimated to be $<100\text{ ms}</math> from the ON-OFF curve, b) Continuous photoswitching measurements of an (N-MPDA)[PbBr₄] crystal with a continuous ON-OFF cycle confirms the device robustness and stability.$

where R_λ , A , q , and I_{dark} are photoresponsivity, effective area, elementary charge, and dark current, respectively.^[53–55] In Figure 3e, the specific detectivity with varying power was estimated. The (N-MPDA)[PbBr₄] possesses a maximum $D^*_{\text{shot}} \approx 1.8 \times 10^{12}$ Jones at 0.15 mW cm^{-2} of 405 nm ($V_g = 0\text{ V}$ and $V_{\text{ds}} = 10\text{ V}$). The obtained D^*_{shot} is better than (AMP)MAPb₂I₇, (BA)₂PbBr₄ and equal to (PEA)₂PbBr₄.^[46,41,42] Normalized gain (Γ_n) is another important figure of merit for a photodetector. It is generally expressed by $\Gamma_n = (E/e) (I_{\text{ph}}/p) (I^2/V)$.^[56,57] We estimated the (N-MPDA)[PbBr₄] gain value in relation to different illumination power, and the maximum obtained value of Γ_n is $\approx 1.24 \times 10^{-5}\text{ V}^{-1}\text{ cm}^2$ (Figure 3f).

Time-resolved ($I_{\text{ds}}-t$) measurements were performed to confirm the robustness and photoswitching stability of the (N-MPDA)[PbBr₄] crystal under light illumination (ON) and dark (OFF) conditions in a room environment. The $I_{\text{ds}}-t$ plot was obtained by illuminating the (N-MPDA)[PbBr₄] with a train of ON-OFF illumination at 405 nm . **Figure 4a** shows the (N-MPDA)[PbBr₄] device response to a single ON-OFF cycle, which displays a fast rise of current (I_{ds}) under illumination followed by a sudden drop after switching off the laser and slow relaxation until it reaches stable. The estimated rising and falling time of the photo-generated signal was found to be $<100\text{ ms}$. The falling time contains two stages a sudden decay of 100 ms and slow relaxation of $\approx 5\text{ s}$. The formation of traps and defects in the as-grown (N-MPDA)[PbBr₄] single crystal might be attributed to the low response time.^[58,59] Consecutive

photoswitching, robustness, and stability of the (N-MPDA)[PbBr₄] device were further examined by an uninterrupted train of ON-OFF illumination for >20 cycles (Figure 4b). The reproducible ON-OFF cycle curve shows no degradation under constant laser illumination and ambient environment, which proves robustness, reproducible response, and switching stability of the (N-MPDA)[PbBr₄] crystal. The high stability of the (N-MPDA)[PbBr₄] crystal is due to the high tolerance factor of long-chain diammonium NMPDA spacer and Br⁻ ion in the crystal structure. Additionally, the Pb–Br bond provides high lattice energy than the iodide-based perovskites, thus avoiding the decomposition of materials.^[60] Overall, the (N-MPDA)[PbBr₄] crystals show outstanding stability against light and moisture, which usually appears to be a daunting challenge in 3D and other 2D perovskite materials.

Random lasers recently exhibited unparalleled interest among researchers due to their potential applications ranging from imaging, sensors, and curved displays.^[61–63] Here, we have also explored the random lasing properties of our (N-MPDA)[PbBr₄] single crystal. Random lasing occurs in strong scattering media,^[62] where the photons are spontaneously emitted and scattered in all directions. The multiple scatterings can form localized loops, which provide coherent feedback to the emission, and thus, random lasing action can be achieved.^[62,64] As displayed in **Figure 5a**, multiple sharp lasing peaks can be observed. The observed lasing modes are spectrally very close, which can be ascribed to their exponential confinement. The

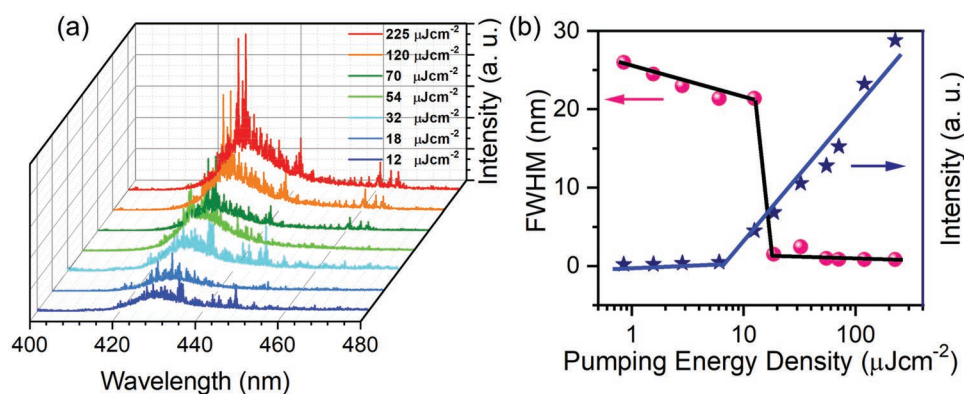


Figure 5. a) The random lasing output of (N-MPDA)[PbBr₄] device with different pump fluence from 12 to $225\text{ }\mu\text{J cm}^{-2}$. b) FWHM and lasing intensity with respect to pumping energy density.

random lasing phenomenon in (N-MPDA)[PbBr₄] can be attributed to our material single-crystal nature, where certain defects behave as scattering centers.^[63] The surface roughness of the 2D perovskite (N-MPDA)[PbBr₄] single crystal was measured using an atomic force microscope (AFM) at a different area. Based on the AFM result, the estimated average surface roughness values at three different locations are 11.3, 14, and 17.6 nm, as shown in Figure S7 (Supporting Information). Typically, surface morphology plays a vital role in random lasing. A smoother surface reduces the loss of incident pump light at the air-crystal surface interface. It increases the fraction of pump light propagating through the crystal, which is highly beneficial for generating amplified spontaneous emissions (ASE).^[65] On the other hand, slight differences in material roughness can benefit random lasing. In addition, the difference in refractive index between the end facets of the perovskites and the surrounding medium can also lead to it behaving as gain media where total internal reflection may lead to effective light trapping.^[66] All the above factors combined to enhance our perovskite device's light-trapping ability.

An essential feature of a random laser is observing a threshold pump intensity during random lasing action, distinguishing it from a thermal source.^[60–62] Figure 5b demonstrates the lasing threshold at 6.5 μJ cm⁻² and a substantial kink as it transits from less than the threshold to higher than the threshold. It is essential to highlight that below the threshold excitation density, the light-matter interaction in the matrix produces a normal distribution of the photogenerated carriers. Population inversion is achieved when the excitation density

crosses the threshold value, thanks to the strong confinement of emitted photon modes. As a result, the perovskites lasing system emits sharp lasing modes, which surplus the spontaneous emission intensity. In addition, as shown in Figure 5b, the FWHM of laser output gets narrower and sharply decreases from ≈20 to 0.1 nm at the threshold value, which results in a high Q factor ≈2673 for our laser devices, as shown in Figure S8 (Supporting Information). Thus, the evolution of the emission spectra (both linewidth and integrated intensity) with pumping intensity carries a firm signature of lasing from the 2D perovskites system. The irregular evolution of peaks and a variable wavelength spacing between two adjacent peaks further strengthen our claim that the observed phenomenon is random lasing (Figure S9, Supporting Information).^[67] Multiple sharp peaks can be seen throughout the spectra, making it a strong candidate for curved display applications. The low threshold and high Q factor can be attributed to three key qualities of our perovskite device: a long mean free path of carriers, high exciton binding energies, and slow auger recombination.^[68–71] Some of these qualities have been previously reported in single-crystal perovskites.^[72,73] We compared our results with various reports of random lasing obtained from different 2D perovskite materials and given in Table S2 (Supporting Information).

To further validate our claims, we studied the angle-dependent lasing phenomenon of our laser device at the same pumping intensity. The device was rotated at different angles ranging from +20° to -20° with respect to the line of incidence of the pumping laser. As depicted in Figure 6a, all three spectra show distinct lasing action with different peak positions, which

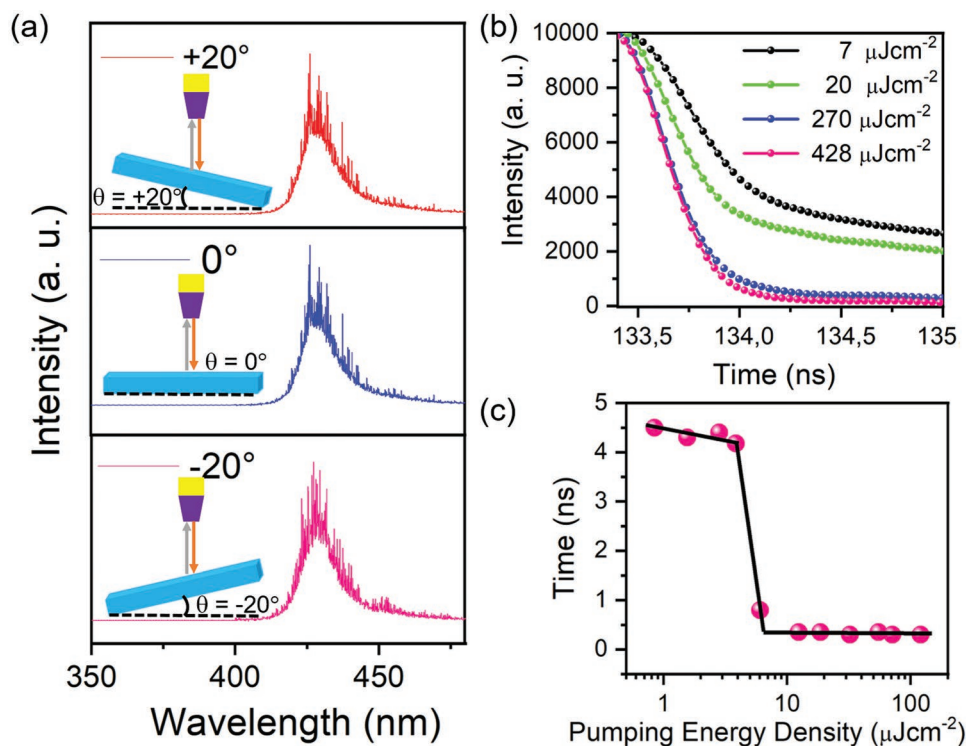


Figure 6. a) Angular dependence emission spectra of (N-MPDA)[PbBr₄] single-crystalline random laser. The angles +20, 0, and -20 degrees have been measured by vertically rotating the sample concerning the line of incidence of the pumping laser as described with the respective spectra. b) Typical decay curves at different pump fluences ranging from PL to random lasing. c) Calculated carrier lifetime of the (N-MPDA)[PbBr₄] single-crystalline laser as a function of pumping energy density. A sharp drop in carrier lifetime (0.3 ns) occurs at the threshold value of pump fluence of 12 μJ cm⁻².

proves the multi-directionality of our random lasing output. The random lasing phenomenon depends on the formation of closed loops. When the angle of incidence changes, the localization path changes, and hence we see different peak positions. It is noteworthy that the number of modes is more when the sample is tilted. This may be due to the increased effective illumination area at tilted angles. A large area gives rise to a high number of modes due to the formation of more closed loops. This is consistent with the random lasing model.^[74,75]

We performed time-resolved photoluminescence (TRPL) studies at different pumping energy densities of the same excitation source to study the dynamic process of lasing action. The obtained decay curves at different pump fluences ranging from PL to random lasing process are illustrated in Figure 6b. At lower pump fluence (below the threshold), the decay profile fitted to an exponential function gives us a carrier lifetime of [≈ 4.5 ns], which decreases to [0.3 ns] when the pump fluence is above the threshold. This indicates a stimulated emission process and lasing action in our single-crystal perovskite device. We plot the calculated excited state carrier lifetime as a function of pump fluence in Figure 6c. Such a sharp drop in the carrier lifetime points to the occurrence of a stimulated emission process and lasing action in our perovskite device. Since there are many available modes, we can expect a low lifetime. It is also known that the radiation density is directly proportional to the recombination rate in the matrix. Hence, the sharp drop in carrier lifetime at the threshold value of pump fluence indicates a stimulated emission process and can be regarded as strong evidence for the lasing action.^[76,77]

3. Conclusion

In summary, the solution-grown 2D (N-MPDA)[PbBr₄] hybrid perovskite single crystal formed by long-chain organic divalent diammonium organic cation shows a stable photodetector with high photoresponsivity and large specific detectivity. These values are much greater than the photodetectors fabricated using monovalent RP-phase 2D (BA)₂PbBr₄ and (PEA)₂PbBr₄ perovskites. As an optical resonator, the single crystal displays a low threshold random lasing with an evolution of sharp lasing spikes of FWHM of 0.1 nm. Based on our results, the solution-grown 2D (N-MPDA)[PbBr₄] crystal with exceptional optoelectronic properties could significantly advance the field of perovskite-based optoelectronics and play an active role in the stability of light-sensing devices and long-life laser applications.

4. Experimental Section

Characterizations: The XRD analysis was performed on Bruker D2 PHASER (CuK α radiation). The TEM, SEM, and EDX mapping were obtained with (JEOL, JEM-2100F) and (FEI, Nova 200) to analyze the morphology and chemical elements of the (N-MPDA)[PbBr₄] single crystal. The active illuminated area of the (N-MPDA)[PbBr₄] photodetector device is 1000 μm^2 . The $I_{\text{ds}}-V_{\text{ds}}$ curves were measured using a source meter (Keithley 2636A) with an optical system including a He-Ne laser (405 nm), power meter (Ophir, Nova II), and bandpass filters. A pulsed laser of wavelength 374 nm was used as the pumping source for studying the lasing spectra and carrier lifetime. The laser

incident area-dependent lasing spectra were acquired using a Horiba-Jobin-Yvon TRIAX 320 spectrometer with 60x (LMPlanFI, Japan) and 100x (Olympus, Japan) objectives. The SHG spectroscopy analysis was performed using a 1064 nm femtosecond laser and a home-built LSCM.

Supporting Information

Supporting Information is available from the Wiley Online Library or from the author.

Acknowledgements

R.K.U. and P.K.R. contributed equally to this work. R.S. acknowledges the Ministry of Science and Technology (MOST), Taiwan, under grant numbers MOST-111-2124-M-001-009, MOST-110-2112-M-001-065-MY3, and Academia Sinica for the budget of AS-iMATE-19-112. C.-T.L. would like to thank the National Science and Technology Council (NSTC), Taiwan, for financial support (grant numbers: NSTC 111-2119-M-002-007, NSTC 111-2622-8-002-001, NSTC 110-2112-M-002-029-MY3, and NSTC 108-2119-M-002-025-MY3). C.-Y.L. acknowledges the grant numbers NSTC-111-2112-M-033-005, NSTC-110-2221-E-033-022, and NSTC 111-2628-E-033-002-MY3. R.C.M. and A.R. acknowledge the Marie Skłodowska-Curie Individual Fellowship (MOFUS, #795356).

Conflict of Interest

The authors declare no conflict of interest.

Data Availability Statement

The data that support the findings of this study are available from the corresponding author upon reasonable request.

Keywords

long-chain spacers, optoelectronics, random lasing, responsivity, second-harmonic generation

Received: January 12, 2023
Published online: February 7, 2023

- [1] A. Kojima, K. Teshima, Y. Shirai, T. Miyasaka, *J. Am. Chem. Soc.* **2009**, *131*, 6050.
- [2] N. J. Jeon, J. H. Noh, Y. C. Kim, W. S. Yang, S. Ryu, S. Seok, *Nat. Mater.* **2014**, *13*, 897.
- [3] C. Luo, W. Li, D. Xiong, J. Fu, W. Q. Yang, *Nanoscale* **2019**, *11*, 15206.
- [4] H. J. Snaith, *J. Phys. Chem. Lett.* **2013**, *4*, 3623.
- [5] P. Calado, A. M. Telford, D. Bryant, X. Li, J. Nelson, B. C. O'Regan, P. R. F. Barnes, *Nat. Commun.* **2016**, *7*, 13831.
- [6] A. Mandal, A. Ghosh, D. Ghosh, S. Bhattacharyya, *ACS Appl. Mater. Interfaces* **2021**, *13*, 43104.
- [7] L. Zheng, K. Wang, T. Zhu, L. Liu, J. Zheng, X. Gong, *ACS Omega* **2019**, *4*, 15873.
- [8] H. Zhu, Y. Fu, F. Meng, X. Wu, Z. Gong, Q. Ding, M. V. Gustafsson, M. T. Trinh, S. Jin, X.-Y. Zhu, *Nat. Mater.* **2015**, *14*, 636.
- [9] G. Hodes, D. Cahen, *Nat. Photonics* **2014**, *8*, 87.
- [10] K. Wang, L. Zheng, T. Zhu, L. Liu, M. L. Becker, X. Gong, *Nano Energy* **2020**, *67*, 104229.

- [11] L. Dou, Y. Yang, J. You, Z. Hong, W.-H. Chang, G. Li, Y. Yang, *Nat. Commun.* **2014**, *5*, 5404.
- [12] T. Zhu, Y. Yang, L. Zheng, L. Liu, M. L. Becker, X. Gong, *Adv. Funct. Mater.* **2020**, *30*, 1909487.
- [13] Q. Zhang, R. Su, W. Du, X. Liu, L. Zhao, S. T. Ha, Q. Xiong, *Small Methods* **2017**, *1*, 1700163.
- [14] M. M. Stylianakis, T. Maksudov, A. Panagiotopoulos, G. Kakavelakis, K. Petridis, *Materials* **2019**, *12*, 859.
- [15] X. Zhang, H. Liu, W. Wang, J. Zhang, B. Xu, K. L. Karen, Y. Zheng, S. Liu, S. Chen, K. Wang, X. W. Sun, *Adv. Mater.* **2017**, *29*, 1606405.
- [16] F. Bella, G. Griffini, J.-P. C. Baena, G. Saracco, M. Gratzel, A. Hagfeldt, S. Turri, C. Gerbaldi, *Science* **2016**, *354*, 203.
- [17] Z. Li, M. Yang, J.-S. Park, S.-H. Wei, J. J. Berry, K. Zhu, *Chem. Mater.* **2016**, *28*, 284.
- [18] S. Zhou, T. Zhu, L. Zheng, D. Zhang, W. Xu, L. Liu, G. Cheng, J. Zheng, X. Gong, *RSC Adv.* **2019**, *9*, 30317.
- [19] F. Zhang, W. Shi, J. Luo, N. Pellet, C. Yi, X. Li, X. Zhao, T. J. S. Dennis, X. Li, S. Wang, Y. Xiao, S. M. Zakeeruddin, D. Bi, M. Gratzel, *Adv. Mater.* **2017**, *29*, 1606806.
- [20] L. Pedesseau, D. Saporì, B. Traore, R. Robles, H.-H. Fang, M. A. Loi, H. Tsai, W. Nie, J.-C. Blancon, A. Neukirch, S. Tretiak, A. D. Mohite, C. Katan, J. Even, M. Kepenekian, *ACS Nano* **2016**, *10*, 9776.
- [21] I. C. Smith, E. T. Hoke, D. Solis-Ibarra, M. D. McGehee, H. I. Karunadasa, *Angew. Chem., Int. Ed.* **2014**, *53*, 11232.
- [22] P. Cheng, Z. Xu, J. Li, Y. Liu, Y. Fan, L. Yu, D.-M. Smilgies, C. Muller, K. Zhao, S. F. Liu, *ACS Energy Lett.* **2018**, *3*, 1975.
- [23] Y. Chen, Y. Sun, J. Peng, J. Tang, K. Zheng, Z. Liang, *Adv. Mater.* **2018**, *30*, 1703487.
- [24] L. Mao, W. Ke, L. Pedesseau, Y. Wu, C. Katan, J. Even, M. R. Wasielewski, C. C. Stoumpos, M. G. Kanatzidis, *J. Am. Chem. Soc.* **2018**, *140*, 3775.
- [25] Z. Xu, D. Lu, X. Dong, M. Chen, Q. Fu, Y. Liu, *Adv. Mater.* **2021**, *33*, 2105083.
- [26] Y. Shang, Y. Liao, Q. Wei, Z. Wang, B. Xiang, Y. Ke, W. Liu, Z. Ning, *Sci. Adv.* **2019**, *5*, aaw8072.
- [27] H. Ye, Y. Peng, X. Shang, L. Li, Y. Yao, X. Zhang, T. Zhu, X. Liu, X. Chen, J. Luo, *Adv. Funct. Mater.* **2022**, *32*, 2200223.
- [28] E. R. Dohner, E. T. Hoke, H. I. Karunadasa, *J. Am. Chem. Soc.* **2014**, *136*, 1718.
- [29] W. Yu, F. Li, L. Yu, M. R. Niazi, Y. Zou, D. Corzo, A. Basu, C. Ma, S. Dey, M. L. Tietze, U. Buttner, X. Wang, Z. Wang, M. N. Hedhili, C. Guo, T. Wu, A. Amassian, *Nat. Commun.* **2018**, *9*, 5354.
- [30] R. K. Ulaganathan, R. C. Murugesan, C.-Y. Lin, A. Subramanian, W.-L. Chen, Y.-M. Chang, A. Rozhin, R. Sankar, *Adv. Funct. Mater.* **2022**, *32*, 2112277.
- [31] E. R. Dohner, A. Jaffe, L. R. Bradshaw, H. I. Karunadasa, *J. Am. Chem. Soc.* **2014**, *136*, 13154.
- [32] C. Wehrenfenning, M. Liu, H. J. Snaith, M. B. Johnston, L. M. Herz, *J. Phys. Chem. Lett.* **2014**, *5*, 1300.
- [33] D. M. Sagar, R. R. Cooney, S. L. Sewall, E. A. Dias, M. M. Barsan, I. S. Butler, P. Kambhampati, *Phys. Rev. B* **2008**, *77*, 235321.
- [34] J. Mooney, M. M. Krause, J. I. Saari, P. Kambhampati, *J. Chem. Phys.* **2013**, *138*, 204705.
- [35] J. Mooney, M. M. Krause, J. I. Saari, P. Kambhampati, *Phys. Rev. B* **2013**, *87*, 081201.
- [36] T. Ikehara, T. Itoh, *Phys. Rev. B* **1991**, *44*, 9283.
- [37] C. C. Stoumpos, D. H. Cao, D. J. Clark, J. Young, J. M. Rondinelli, J. I. Jang, J. T. Hupp, M. G. Kanatzidis, *Chem. Mater.* **2016**, *28*, 2852.
- [38] D. J. Morrow, M. P. Hautzinger, D. P. Lafayette, J. M. Scheeler, L. Dang, M. Leng, D. D. Kohler, A. M. Wheaton, Y. Fu, I. A. Guzei, J. Tang, S. Jin, J. C. Wright, *J. Phys. Chem. Lett.* **2020**, *11*, 6551.
- [39] R. Dong, C. Lan, F. Li, S. Yip, J. C. Ho, *Nanoscale Horiz.* **2019**, *4*, 1342.
- [40] L. Qian, Y. Sun, M. Sun, Z. Fang, L. Li, D. Xie, C. Li, L. Ding, *J. Mater. Chem. C* **2019**, *7*, 5353.
- [41] E. Choi, Y. Zhang, A. M. Soufiani, M. Lee, R. F. Webster, M. E. Pollard, P. J. Reece, W. Lee, J. Seidel, J. Lim, J.-H. Yun, J. S. Yun, *npj 2D Mater. Appl.* **2022**, *6*, 43.
- [42] F. Ledee, A. Ciavatti, M. Verdi, L. Basiricò, B. Fraboni, *Adv. Opt. Mater.* **2022**, *10*, 2101145.
- [43] T. Liu, W. Shi, W. Tang, Z. Liu, B. C. Schroeder, O. Fenwick, M. J. Fuchter, *ACS Nano* **2022**, *16*, 2682.
- [44] L. Min, W. Tian, F. Cao, J. Guo, L. Li, *Adv. Mater.* **2021**, *33*, 2101714.
- [45] Q. Wang, Q. Zhang, X. Luo, J. Wang, R. Zhu, Q. Liang, L. Zhang, J. Z. Yong, C. P. Y. Wong, G. Eda, J. H. Smet, A. T. S. Wee, *ACS Appl. Mater. Interfaces* **2020**, *12*, 45235.
- [46] I.-H. Park, K. C. Kwon, Z. Zhu, X. Wu, R. Li, Q.-H. Xu, K. P. Loh, *J. Am. Chem. Soc.* **2020**, *142*, 18592.
- [47] W. Wu, X. Wang, X. Han, Z. Yang, G. Gao, Y. Zhang, J. Hu, Y. Tan, A. Pan, C. Pan, *Adv. Mater.* **2019**, *31*, 1805913.
- [48] S. Ahmad, P. Fu, S. Yu, Q. Yang, X. Liu, X. Wang, X. Guo, C. Li, *Joule* **2019**, *3*, 794.
- [49] X. Zhang, L. Xu, M. Chen, Y. Kang, J. Lei, Q. Wu, C. Sun, Z. Lin, P. Wang, Z. Yang, *Solid State Commun.* **2022**, *350*, 114761.
- [50] Y. Zhong, G. Liu, Y. Su, W. Sheng, L. Gong, J. Zhang, L. Tan, Y. Chen, *Angew. Chem.* **2022**, *134*, 202114588.
- [51] D. Ghosh, D. Acharya, L. Pedesseau, C. Katan, J. Even, S. Tretiak, A. J. Neukirch, *J. Mater. Chem. A* **2020**, *8*, 22009.
- [52] S. Yu, M. Abdellah, T. Pullerits, K. Zheng, Z. Liang, *Adv. Funct. Mater.* **2021**, *31*, 2104342.
- [53] Z. Wu, N. Li, N. Eedugurala, J. D. Azoulay, D.-S. Leem, T. N. Ng, *Npj Flexible Electron.* **2020**, *4*, 6.
- [54] K. Wang, X. Qiu, Z. Lv, Z. Song, H. Jiang, *Photonics Res.* **2022**, *10*, 111.
- [55] X. Gong, M. Tong, Y. Xia, W. Cai, J. S. Moon, Y. Cao, G. Yu, C.-L. Shieh, B. Nilsson, A. J. Heeger, *Science* **2009**, *325*, 1665.
- [56] S. Ghosh, W. C. Chiang, M. Y. Fakhri, C. T. Wu, R. S. Chen, S. Chattopadhyay, *Nano Energy* **2020**, *67*, 104258.
- [57] H.-W. Yang, H.-F. Hsieh, R.-S. Chen, C.-H. Ho, K.-Y. Lee, L.-C. Chao, *ACS Appl. Mater. Interfaces* **2018**, *10*, 5740.
- [58] W.-J. Yin, T. Shi, Y. Yan, *Appl. Phys. Lett.* **2014**, *104*, 063903.
- [59] J. Kim, S.-H. Lee, J. H. Lee, K.-H. Hong, *J. Phys. Chem. Lett.* **2014**, *5*, 1312.
- [60] A. Aziz, N. Aristidou, X. Bu, R. J. E. Westbrook, S. A. Haque, M. S. Islam, *Chem. Mater.* **2020**, *32*, 400.
- [61] N. M. Lawandy, R. M. Balachandran, A. S. L. Gomes, E. Sauvain, *Nature* **1994**, *368*, 436.
- [62] D. S. Wiersma, *Nat. Phys.* **2008**, *4*, 359.
- [63] Y. Liu, W. Yang, S. Xiao, N. Zhang, Y. Fan, G. Qu, Q. Song, *ACS Nano* **2019**, *13*, 10653.
- [64] P. K. Roy, G. Haider, H.-I. Lin, Y.-M. Liao, C.-H. Lu, K.-H. Chen, L.-C. Chen, W.-H. Shih, C.-T. Liang, Y.-F. Chen, *Adv. Opt. Mater.* **2018**, *6*, 1800382.
- [65] C. Li, Z. Zang, C. Han, Z. Hu, X. Tang, J. Du, Y. Leng, K. Sun, *Nano Energy* **2017**, *40*, 195.
- [66] X. Zhuang, Y. Ouyang, X. Wang, A. Pan, *Adv. Opt. Mater.* **2019**, *7*, 1900071.
- [67] Z.-F. Shi, X.-G. Sun, D. Wu, T.-T. Xu, Y.-T. Tian, Y.-T. Zhang, X.-J. Li, G.-T. Du, *J. Mater. Chem. C* **2016**, *4*, 8373.
- [68] S. Yakunin, L. Protesescu, F. Krieg, M. I. Bodnarchuk, G. Nedelcu, M. Humer, G. De Luca, M. Fiebig, W. Heiss, M. V. Kovalenko, *Nat. Commun.* **2015**, *6*, 8056.
- [69] I. Robel, R. Gresback, U. Kortshagen, R. D. Schaller, V. I. Klimov, *Phys. Rev. Lett.* **2009**, *102*, 177404.
- [70] H. Zhu, Y. Fu, F. Meng, X. Wu, Z. Gong, Q. Ding, M. V. Gustafsson, M. T. Trinh, S. Jin, X. Y. Zhu, *Nat. Mater.* **2015**, *14*, 636.
- [71] J.-C. Blancon, H. Tsai, W. Nie, C. C. Stoumpos, L. Pedesseau, C. Katan, M. Kepenekian, C. M. M. Soe, K. Appavoo, M. Y. Sfeir, S. Tretiak, P. M. Ajayan, M. G. Kanatzidis, J. Even, J. J. Crochet, A. D. Mohite, *Science* **2017**, *355*, 1288.

- [72] P. K. Roy, R. K. Ulaganathan, C. M. Raghavan, S. M. Mhatre, H.-I. Lin, W.-L. Chen, Y.-M. Chang, A. Rozhin, Y.-T. Hsu, Y.-F. Chen, R. Sankar, F.-C. Chou, C.-T. Liang, *Nanoscale* **2020**, *12*, 18269.
- [73] C. M. Raghavan, T.-P. Chen, S.-S. Li, W.-L. Chen, C.-Y. Lo, Y.-M. Liao, G. Haider, C.-C. Lin, C.-C. Chen, R. Sankar, Y.-M. Chang, F.-C. Chou, C.-W. Chen, *Nano Lett.* **2018**, *18*, 3221.
- [74] Y. Ling, H. Cao, A. L. Burin, M. A. Ratner, X. Liu, R. P. H. Chang, *Phys. Rev. A* **2001**, *64*, 063808.
- [75] H. Cao, Y. G. Zhao, S. T. Ho, E. W. Seelig, Q. H. Wang, R. P. H. Chang, *Phys. Rev. Lett.* **1999**, *82*, 2278.
- [76] H.-W. Hu, G. Haider, Y.-M. Liao, P. K. Roy, R. Ravindranath, H.-T. Chang, C.-H. Lu, C.-Y. Tseng, T.-Y. Lin, W.-H. Shih, Y.-F. Chen, *Adv. Mater.* **2017**, *29*, 1703549.
- [77] G. Haider, R. Ravindranath, T.-P. Chen, P. Roy, P. K. Roy, S.-Y. Cai, H.-T. Chang, Y.-F. Chen, *Nat. Commun.* **2017**, *8*, 256.